minerals

MDPI

Article

Geochemistry of Basalts from Southwest Indian Ridge 64° E: Implications for the Mantle Heterogeneity East of the Melville Transform

Zhen Dong [1,2,3], Chunhui Tao [2,3,4,*], Jin Liang [2,3,*], Shili Liao [2,3], Wei Li [2,3], Guoyin Zhang [2,3] and Zhimin Cao [1]

[1] College of Marine Geosciences, Ocean University of China, Qingdao 266100, China; dongzhen@stu.ouc.edu.cn (Z.D.); zmcao@ouc.edu.cn (Z.C.)
[2] Key Laboratory of Submarine Geosciences, Ministry of Natural Resources, Hangzhou 310012, China; liaosl@sio.org.cn (S.L.); goofyji@126.com (W.L.); zhanggy@sio.org.cn (G.Z.)
[3] Second Institute of Oceanography, Ministry of Natural Resources, Hangzhou 310012, China
[4] School of Oceanography, Shanghai Jiao Tong University, Shanghai 200030, China
* Correspondence: taochunhuimail@163.com (C.T.); esljin@163.com (J.L.)

Abstract: As one of the regional, magmatic, robust, axial ridge segments along the ultraslow-spreading Southwest Indian Ridge (SWIR), the magmatic process and mantle composition of the axial high relief at 64° E is still unclear. Here, we present major and trace elements and Sr-Nd-Pb isotope data of mid-ocean ridge basalts (MORBs) from 64° E. The basalts show higher contents of Al_2O_3, SiO_2, and Na_2O and lower contents of TiO_2, CaO, and FeO for a given MgO content, and depletion in heavy rare-earth elements (HREE), enrichment in large-ion lithophile elements, and lower $^{87}Sr/^{86}Sr$, $^{143}Nd/^{144}Nd$ and higher radiogenic Pb isotopes than the depleted MORB mantle (DMM). The high Zr/Nb (24–43) and low Ba/Nb (3.8–7.0) ratios are consistent with typical, normal MORB (N-MORB). Extensive plagioclase fractional crystallization during magma evolution was indicated, while fractionation of olivine and clinopyroxene is not significant, which is consistent with petrographic observations. Incompatible trace elements and isotopic characteristics show that the basaltic melt was formed by the lower partial melting degree of spinel lherzolite than that of segment #27 (i.e., Duanqiao Seamount, 50.5° E), Joseph Mayes Mountain (11.5° E), etc. The samples with a DMM end-member are unevenly mixed with the lower continental crust (LCC)- and the enriched mantle end-member (EM2)-like components, genetically related to the Gondwana breakup and contaminated by upper and lower continental crust (or continental mantle) components.

Keywords: Sr–Nd–Pb isotopes; mantle melting; mantle heterogeneity; end-member mixing

check for updates

Citation: Dong, Z.; Tao, C.; Liang, J.; Liao, S.; Li, W.; Zhang, G.; Cao, Z. Geochemistry of Basalts from Southwest Indian Ridge 64° E: Implications for the Mantle Heterogeneity East of the Melville Transform. *Minerals* **2021**, *11*, 175. https://doi.org/10.3390/min11020175

Academic Editor: Alexandre V. Andronikov
Received: 11 January 2021
Accepted: 28 January 2021
Published: 8 February 2021

Publisher's Note: MDPI stays neutral with regard to jurisdictional claims in published maps and institutional affiliations.

Copyright: © 2021 by the authors. Licensee MDPI, Basel, Switzerland. This article is an open access article distributed under the terms and conditions of the Creative Commons Attribution (CC BY) license (https://creativecommons.org/licenses/by/4.0/).

1. Introduction

Defined by a seafloor full spreading rate of <20 mm/year, the ultraslow-spreading ridges constitute 36% of the 55,000 km global mid-ocean ridge system [1]. Among these ridges, the Southwest Indian Ridge (SWIR) is characterized by an almost uniform plate separation rate of ~14 mm/year [2] along its entire length with variation in segmentation, spreading obliquity, and axial morphology [3]. Regionally magmatic robust segments with high axial relief and low mantle Bouguer anomaly (MBA) have been observed along the axis of the SWIR, e.g., the Joseph Mayes Seamount (JMS, 11.5° E) in the west; segment #27 (50.5° E) in the middle; and segments #8, #11, and #14 in the east [1,4,5]. These ranges always show a high bathymetric relief and low mantle Bouguer anomaly (MBA) domain, separated by the extensively tectonized sections. The effect of melt/mantle interactions on the composition of erupted basalts and the heterogeneity in the mantle source have attracted considerable attention [6–9].

The oceanic ridge east of the Melville Fracture Zone (MFZ) is characterized by an exceedingly deep axial valley (~4730 m on average), thick lithosphere, and thin oceanic crust (4–5 km on average) [10–13], lower than that of the ridge west of the MFZ (6–7 km on average) [10].

These attributes have been interpreted to reflect a weak magma supply from an underlying cold mantle [14]. Previous studies on the composition of mid-ocean ridge basalts (MORBs) from the eastern SWIR (E-SWIR) showed that their chemical and isotopic composition are different from those of the southern Central Indian Ridge (S-CIR), western Southeast Indian Ridge (W-SEIR), and the Rodrigues Triple Junction (RTJ) [6,15–18]. The isotopic indicator (i.e., lowest $^{206}Pb/^{204}Pb$ values; high $^{87}Sr/^{86}Sr$, $^{207}Pb/^{204}Pb$, and $^{208}Pb/^{204}Pb$; and low $^{143}Nd/^{144}Nd$) showed that the DUPAL [19,20] signal of the E-SWIR axis has a certain peculiarity from the Pacific and north Atlantic [6,14]. Numerous studies have focused on the mantle source and magmatic process characteristics along the E-SWIR [3,7,8,21–23] and discussed different extents of partial melting, fractionation of clinopyroxene, and melt/mantle interaction [9]. The E-SWIR was discovered as a distinct isotopic province, although there was no clear definition of its extension to the west [8].

The 64° E of SWIR covers a typical axial high relief (i.e., Mt. Jourdanne), with two hydrothermal fields (i.e., Tiancheng and Tianzuo) nearby (Figure 1), but the mantle composition and magmatic process beneath are still unclear. This study presents new geochemical data of MORBs from 64° E, including Sr–Nd–Pb isotopes. We conduct geochemical comparisons among MORBs from JMS (11.5° E), 50.5° E (segment #27) of SWIR, E-SWIR, S-CIR, W-SEIR, and RTJ to investigate their petrogenesis and magmatic process and propose some new and detailed insights into the diversity of mantle source composition and mantle mixing end-members.

2. Geological Setting

The E-SWIR is characterized by a common departure from the isostatic compensation of seafloor topography and a pronounced asymmetry of crustal thickness and seafloor relief between the two ridge flanks [4]. Serpentinized peridotites are occasionally exposed within the fracture zones when added to outcropping gabbro and basaltic rocks along larger fault zones [5], as a result of detachment faulting on both sides of the ridge axis [23]. Gravity-derived crustal thickness is approximately 6.3 km underlying the center of high relief segment #11, which is 3–4 km thicker than that of the center of low-relief segments #9 and #10 [4]. No long-lived fracture zones or non-transform discontinuities exist [12,13] (Figure 1b). Detailed surveys indicate that this part of the ridge's heterogeneous seafloor comprises volcanic and ultramafic seafloor areas, where plate separation is accommodated by a large offset of faults [5]. The evidence of a predominance of tectonic over magmatic extensional processes could be related to the unstable and weak, locally focalized magma supply [24].

The study area (27°51′ S, 63°56′ E) is located at the center of segment #11 (Figure 1c), called Mt. Jourdanne [25] with an axial-summit rise of around 1 km above the surrounding median valley flanks (Figure 1c). It is a large volcanic massif (Figure 1d), which has an approximately W–E treading volcanic construction with a lenticular shape and extends for several kilometers along the rift axis [4]. The summit of Mt. Jourdanne is composed of a series of extrusive units, principally alternating sheet flows, lobate flows, tubes, and pillow basalts, which comprise the main outcrop of the northeastern part of the axial volcano ridge [20]. The sheet flows predominate on the smoothly dipping flanks to the north, whereas the pillow mounds and basaltic rock fragments are more dominant on the uppermost plateau of the summit [26]. The straight volcanic ridge is bounded by a non-transform offset at 63°40′ E to the west and 64°10′ E to the east [27].

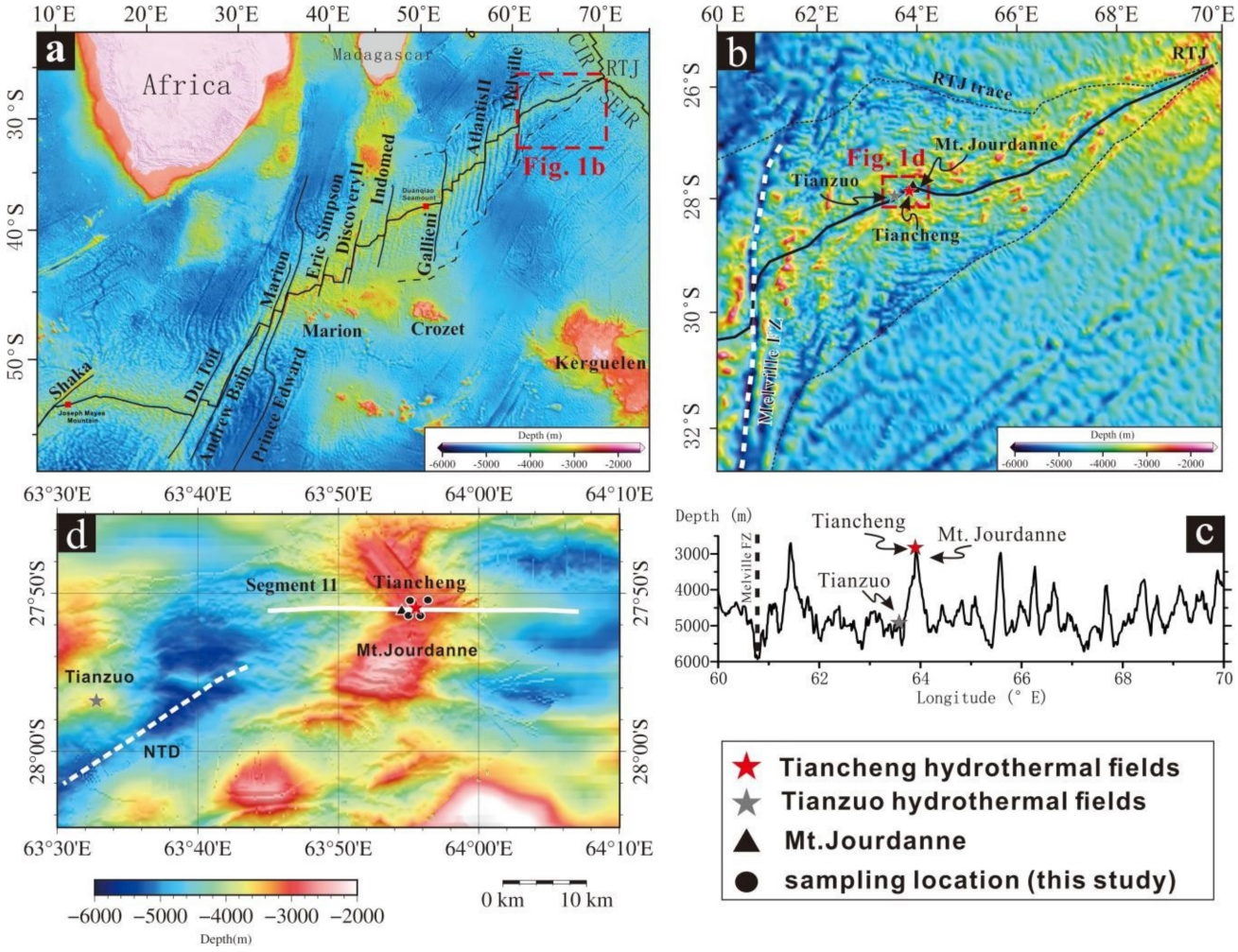

Figure 1. (**a**) The geotectonic setting and topography of the Southwest Indian Ridge (SWIR). (**b**) The area between the Melville Fracture Zone and Rodrigues Triple Junction. (**c**) Along-axis bathymetric profile between 61° E and 69° E. (**d**) Topography of the Tianzuo hydrothermal field and the adjacent Tiancheng and Mt. Jourdanne fields from multibeam sonar data. Subfigures (**a**–**d**) are modified from [28].

3. Sampling and Petrography

The samples were collected from around 27.85° S, 63.92° E using a submersible Jiaolong during the DY125-35 cruise in 2014 (Figure 1c). The quasi-black surface is composed of brown iron and manganese oxides (Figure 2) and a glassy rim with less than 1 cm thickness (Figure 2b). Plagioclase phenocrysts, about 1 cm long, were observed on hand specimens. Thin sections of the fresh samples showed that some samples are composed of aphanitic glass with plagioclases and olivine phenocrysts (Figure 2c,e). The others contain interstitial pyroxene in triangular lattices composed of acicular plagioclase (Figure 2d,e). Vesicular structure and variolitic glass were observed occasionally (Figure 2f).

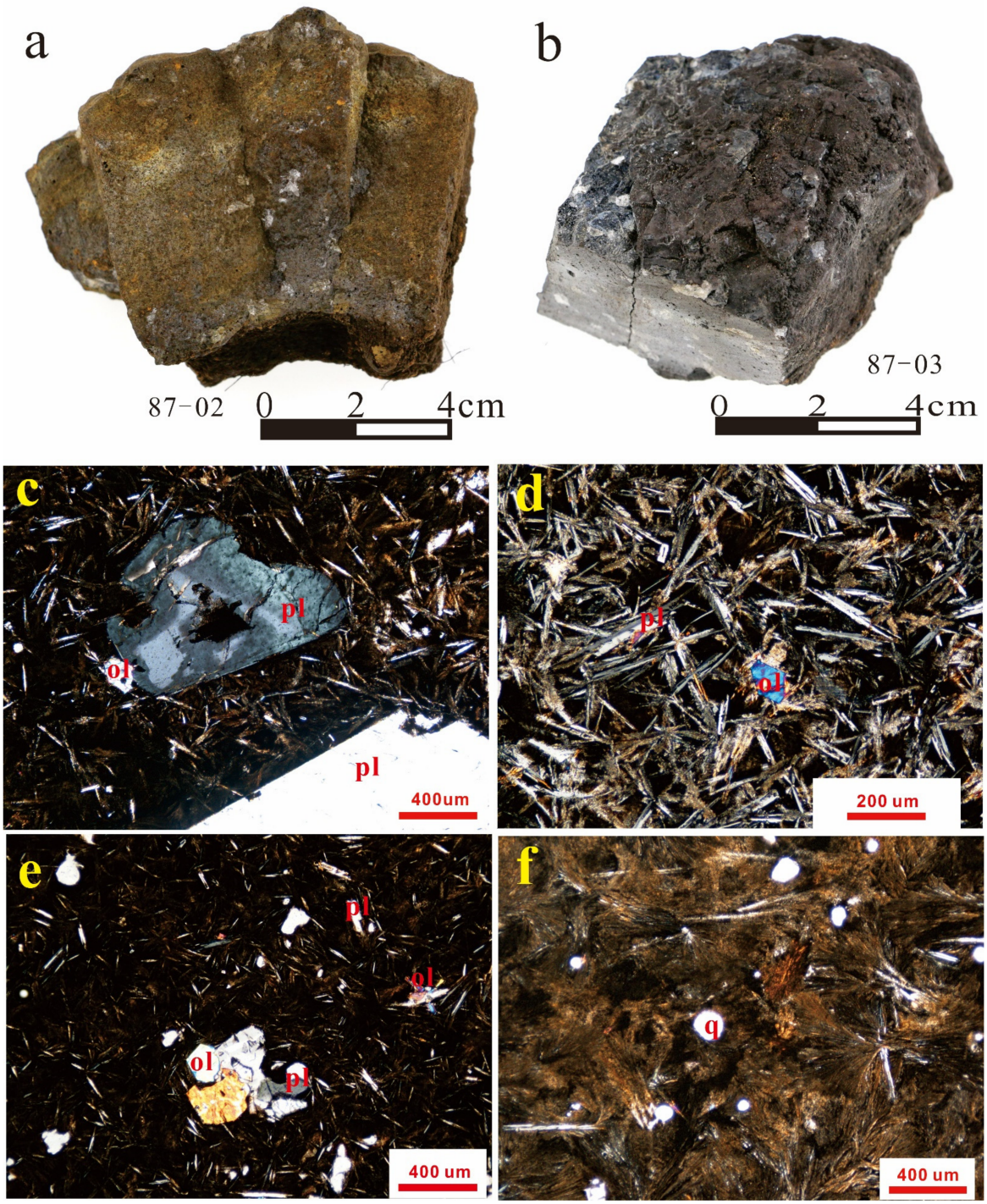

Figure 2. Photographs of hand specimens (**a**,**b**) and their photomicrographs (**c**–**f**) of mid-ocean ridge basalts (MORBs) samples from 64° E; (**c**) plagioclase phenocrysts in a glassy matrix; (**d**) quenched plagioclase laths in glassy MORB; (**e**) olivine phenocrysts in a glassy matrix; (**f**) vesicular structure filled with quartz. (pl = Plagioclase; ol = Olivine).

4. Analytical Methods

Fresh MORB samples were selected for bulk major and trace element analysis, which was performed by ALS Minerals in Guangzhou, China. Major elements were obtained using X-ray fluorescence spectroscopy (XRF). Powdered samples were ignited at 950 °C and mixed with $Li_2B_4O_7$ flux. A loss-on-ignition (LOI) at 1000 °C may be undertaken with the elemental analysis by either Trans-Atlantic Geotraverse (TGA) or manual gravimetric method. The analytical precision was better than ±2–5%. Trace elements were obtained

by using inductively coupled plasma mass spectrometry (ICP-MS). Two rock standards (kinzingite SARM-45 and kiorite Gneiss SY-4) and two randomly selected repeat MORB samples were chosen to monitor the data quality and reproducibility. The analytical precision for most of the trace elements was better than ±5%.

Whole-rock Sr–Nd–Pb isotopic composition was obtained by using a Finnigan MAT-262 mass spectrometer at the Laboratory for Radiogenic Isotope Geochemistry, University of Science and Technology of China. For Nd–Sr isotope analyses, Rb–Sr and light rare-earth elements (REEs) were isolated on quartz columns by conventional ion-exchange chromatography with a 5 mL resin bed of AG 50W-X12 (200–400 mesh). Nd and Sm were separated from other REEs on quartz columns by using 1.7 mL Teflon powder as the cation exchange medium. For isotopic measurements, Sr was loaded with a Ta–HF activator on preconditioned W filaments and was measured in a single-filament mode. Nd was loaded on Re filaments and measured in a double-filament configuration. The measured Sr and Nd isotopic ratios were normalized for mass fractionation by setting $^{86}Sr/^{88}Sr = 0.1194$ and $^{146}Nd/^{144}Nd = 0.7219$, respectively. For Pb isotope determination, 200 mg of sample material was dissolved in HF–HNO_3 acid at 120 °C for 7 days by using Teflon vials. Pb was separated by anion-exchange chromatography with diluted HBr acid as the elutant. During the analyses, the NBS987 Sr isotope standard yielded an $^{87}Sr/^{88}Sr$ value of 0.710266 ± 0.000006 (2σ, n = 2). The measured Nd isotope standard Thermo Nd yielded a $^{143}Nd/^{144}Nd$ ratio of 0.512420 ± 0.000009 (2σ, n = 2). The measured $^{206}Pb/^{204}Pb$, $^{207}Pb/^{204}Pb$, and $^{208}Pb/^{204}Pb$ ratios of standard NBS981 were 16.9374 ± 0.0085, 15.4916 ± 0.0076, and 36.7219 ± 0.0182 (2σ, n = 2), respectively. The standard deviations have been reported from the repeated analysis of each sample.

5. Results

5.1. Major Elements

Table 1 shows the major element data of the 64° E basalts. The samples were relatively fresh, with a low LOI and a narrow range of $Mg^{\#}$ (61.93–62.13) and were classified into the low-K series with K_2O contents of 0.19–0.27 wt.%. They are rich in Al, with Al_2O_3 content reaching as high as 16.78–17.96 wt.%, which is comparable to that of the high-Al MORB (15.62–17.41 wt.%) reported from the center of segment #27 [29]. The MgO content of the samples from 64° E is relatively high (approximately 7–8 wt.%).

Compared with the basalt from segment #27 and JMS, the samples from the study area have relatively higher SiO_2, Al_2O_3, and Na_2O contents (Figure 3a,c,e) and lower TiO_2, CaO, and FeO contents (Figure 3b,d,f) at a given MgO. The Na_2O, K_2O, and TiO_2 contents of the samples decreased with the increase of the MgO content, while the contents of SiO_2, Al_2O_3, and CaO were relatively uniform for all samples (Figure 3).

Table 1. Major element compositions of basalts from the 64° E (wt.%).

Samples	87-S01	87-S02	87-S03	87-S06	DUF0107-016 *	DUF0107-016-002-001 *	DUF107-016 VRAC *	DUF107-016-001-001 *	DUF107-016-002-001 *	DUF107-016-002-003 *	DUF107-016-003-001 *
Longitude (° E)	63.927	63.923	63.926	63.9267	63.91	63.91	63.91	63.91	63.91	63.91	63.91
Latitude (°S)	27.8511	27.8512	27.8511	27.8508	−27.85	−27.85	−27.85	−27.85	−27.85	−27.85	−27.85
Depth (m)	−2839	−2762	−2762	−2816	−2800	−2800	−2800	−2800	−2800	−2800	−2800
SiO_2	50.90	51.12	50.74	50.57	51.44	51.88	50.92	50.95	51.28	51.34	51.34
TiO_2	1.23	1.18	1.14	1.22	1.24	1.38	1.25	1.15	1.29	1.25	1.32
Al_2O_3	16.94	17.33	17.96	17.20	16.93	16.78	16.79	17.01	17.01	17.04	17.13
Fe_2O_3	7.95	7.80	7.32	7.84	7.38	7.73	7.48	7.88	7.95	8.01	7.89
MnO	0.14	0.13	0.13	0.13	0.15	0.14	0.15	0.12	0.15	0.11	0.08
MgO	7.26	7.16	6.73	6.99	7.91	7.54	7.92	7.79	7.37	7.51	7.46
CaO	10.84	10.79	11.05	10.88	10.64	10.64	10.82	11.35	10.9	10.94	10.87
K_2O	0.27	0.19	0.20	0.27	0.19	0.24	0.2	0.12	0.19	0.19	0.19
Na_2O	3.92	3.86	3.91	3.86	3.95	4.03	4	3.63	3.86	3.77	3.81
P_2O_5	0.14	0.13	0.14	0.14	0.15	0.22	0.16	0.13	0.14	0.14	0.16
LOI	0.40	−0.40	−0.20	0.00	-	-	-	-	-	-	-
Total	100.01	99.29	99.11	99.11	99.98	100.58	99.69	100.13	100.14	100.3	100.25
$Mg^{\#}$	61.98	62.13	61.94	61.93	65.57	63.41	65.29	63.72	62.22	62.49	62.68

Note: $Mg^{\#} = (Mg/Mg + Fe^{2+}) \times 100$; * sample from [9].

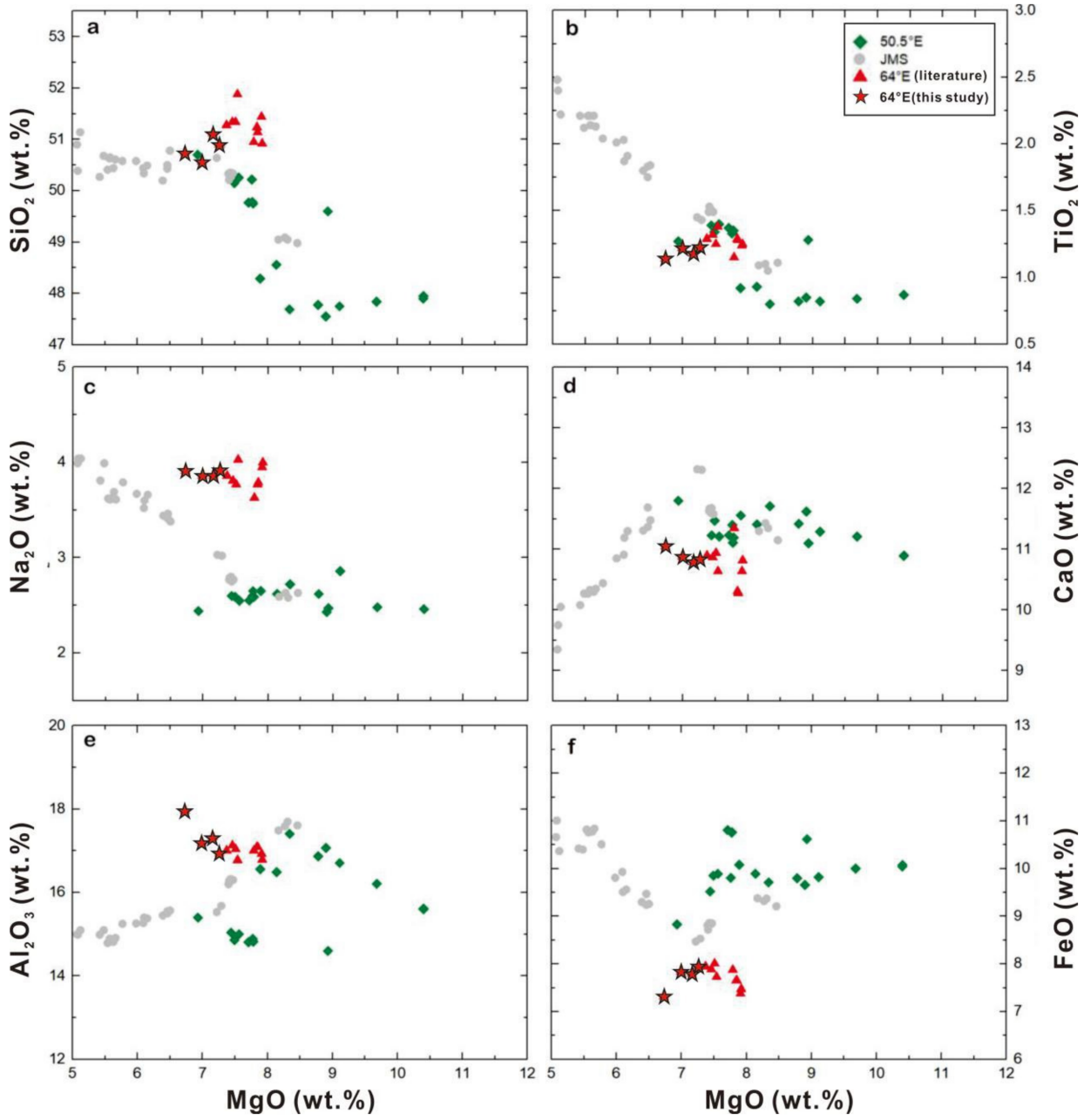

Figure 3. Major oxides vs. MgO diagrams (all in wt.%). Variation of (**a**) SiO_2, (**b**) TiO_2, (**c**) Na_2O, (**d**) CaO, (**e**) Al_2O_3, (**f**) FeO against MgO. The data of 50.5° E and Joseph Mayes Mountain (JMS) basalts for comparison are from PetDB (http://www.petdb.org/). Samples in references covering 64° E were counted [9,14,26].

5.2. Trace Elements

The trace element compositions are given in Table 2. The chondrite-normalized REE diagram (Figure 4a) shows that samples from the 64° E are somewhat enriched in light REEs (LREEs), i.e., $(La/Sm)_N$ = 0.79–1.02, while the heavy REE (HREE) patterns show a weak depletion similar to N-MORB. Basalts collected from MFZ to RTJ were almost all enriched LREEs with average $(La/Sm)_N$ = 0.94 (0.50–1.37, n = 91, and 46% of them with $(La/Sm)_N > 1$). They significantly differed from those from the RTJ with average $(La/Sm)_N$ = 0.61 (0.29–0.83, n = 17) and from those from the Indomed Fracture Zone to the Gallieni Fracture Zone with average $(La/Sm)_N$ = 0.51 (0.38–0.80, n = 43).

Table 2. Trace element compositions of basalts from the 64° E (ppm).

Samples	87-S01	87-S02	87-S03	87-S06	DUF107-016-001-001 *	DUF107-016-002-003 *	DUF107-016-003-001 *
Sc	35.2	34.2	32.5	34.3	-	38.6	-
V	199	192	185	197	213	228.9	300.6
Cr	202	205	192	182	334.5	357.7	298
Co	109.5	232	154.5	99.2	37.7	39.8	41
Ni	93	88.5	85.8	84.4	99.4	105.1	111.3
Cu	61.5	76.5	60.4	53.5	84	77.2	63.9
Zn	55	54	51	55	71.95	62.34	89.81
Rb	1	0.6	0.5	2.1	1.84	1.84	1.14
Sr	203	214	225	208	222.99	221.13	145.85
Y	24.3	22.6	21.9	24	25.4	32.44	35.78
Zr	117.5	107	106.5	114.5	109.46	98.69	126.38
Nb	3.6	4.4	3.3	3.8	2.9	3.21	3.54
Ba	19.9	20.4	20.1	19.8	20.5	20.1	13.43
Hf	2.4	2.2	2.2	2.4	2.18	2.22	3.19
Ta	0.65	2.66	0.83	1.19	0.23	0.21	0.29
Th	0.3	0.3	0.26	0.27	0.23	0.23	0.18
U	0.12	0.13	0.1	0.1	-	0.08	0.1
La	4.4	3.8	3.7	4.6	4.79	4.72	4.71
Ce	14	11.5	11.1	14.5	14.29	13.83	13.86
Pr	1.93	1.9	1.87	1.87	2.2	2.03	2.27
Nd	9.4	9.6	9.5	9.3	11.59	10.23	11.97
Sm	2.89	2.73	2.83	2.9	3.21	2.98	3.86
Eu	1.06	1.11	1.14	1.11	1.11	1.14	1.48
Gd	3.62	3.7	3.4	3.38	3.36	4.05	5.18
Tb	0.62	0.63	0.65	0.65	0.64	0.73	0.86
Dy	4.26	4.18	4.01	3.95	4.1	4.59	6.01
Ho	0.93	0.84	0.89	0.88	0.9	0.97	1.24
Er	2.37	2.41	2.46	2.41	2.48	2.8	3.41
Tm	0.36	0.36	0.36	0.37	0.39	0.43	0.55
Yb	2.46	2.37	2.37	2.18	2.49	2.73	3.47
Lu	0.33	0.31	0.33	0.33	0.37	0.41	0.53
ΣREE	48.63	45.44	44.61	48.43	51.92	51.64	59.4
$(La/Sm)_N$	0.95	0.84	0.81	1.00	0.96	1.02	0.79
$(La/Yb)_N$	1.32	1.14	1.11	1.34	1.38	1.24	0.97

Note: $(La/Sm)_N$ and $(La/Yb)_N$ are chondrite-normalized values according to [30]; * sample from [9]. REE, rare-earth element.

For the trace elements, the primary-mantle-normalized incompatible-element diagram (Figure 4b) shows that the basalts from 64° E have similar patterns to those of N-MORBs. However, the large-ion lithophile elements (LILEs) are slightly more enriched than in N-MORBs. These samples show high Zr/Nb (24–43) and low Ba/Nb (3.8–7.0) ratios, which are characteristics associated with N-MORBs [31].

5.3. Sr–Nd–Pb Isotope

The Sr–Nd–Pb isotope data are given in Table 3. The isotopic ratios from different areas (i.e., E-SWIR, S-CIR, W-SEIR, RTJ, and 64° E) are displayed in Figure 5. The $^{87}Sr/^{86}Sr$ ratios of the basalts from 64° E are in the slightly variable range of 0.702784–0.703510, whereas the $^{143}Nd/^{144}Nd$ ratios with little difference of 0.512998–0.513107 (Figure 5a). The $^{206}Pb/^{204}Pb$, $^{207}Pb/^{204}Pb$, and $^{208}Pb/^{204}Pb$ ratios of the 64° E basalts are 17.8708–17.9287, 15.5150–15.5454, and 37.9753–38.0601, respectively. The Pb isotopic ratios from 64° E is slightly higher than that from the RTJ, W-SEIR, and S-CIR.

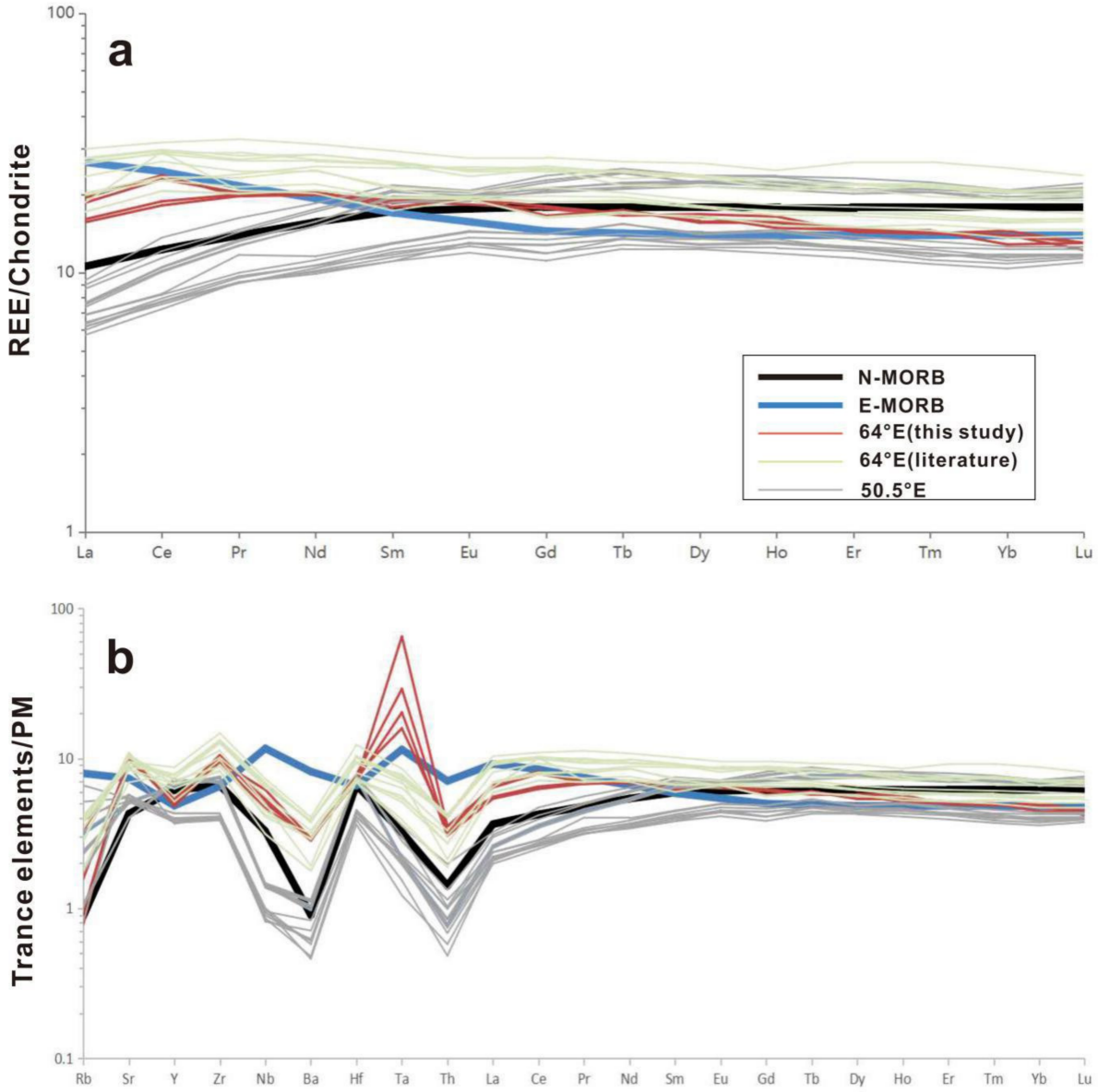

Figure 4. Chondrite-normalized rare-earth elements diagram (**a**) and primary-mantle-normalized spider diagram (**b**). The chondrite, primary mantle, normal MORB (N-MORB), and enriched MORB (E-MORB) are from [30]. Samples in literature covering 64° E were from [9,14,26], and the 50.5° E samples were from [29].

Table 3. Sr–Nd–Pb isotope compositions of basalts from the 64° E.

Samples	$^{87}Sr/^{86}Sr$	$^{143}Nd/^{144}Nd$	$^{206}Pb/^{204}Pb$	$^{207}Pb/^{204}Pb$	$^{208}Pb/^{204}Pb$
87-S01	0.702906	0.513107	17.9287	15.5404	38.0601
87-S02	0.702784	0.513079	17.8708	15.515	37.9912
87-S03	0.703510	0.512998	17.8936	15.5454	37.9913
87-S06	0.702857	0.513073	17.9028	15.5436	37.9753
DUF0107-016 [9]	0.702777	0.51307	17.8	15.43	37.63
DUF0107-016-001-001 [9]	0.702777	0.513077	17.8	15.44	37.65
DUF0107-016-003-001 [9]	0.702777	0.513079	17.82	15.44	37.68
DY0115-017-005A [26]	0.702949	0.513057	18.001	15.615	38.067
DY0115-019-007 [26]	0.702942	0.513061	17.793	15.424	37.612
SHK0446-001 [32]	0.702751	0.513076	17.7921	15.4389	37.6525

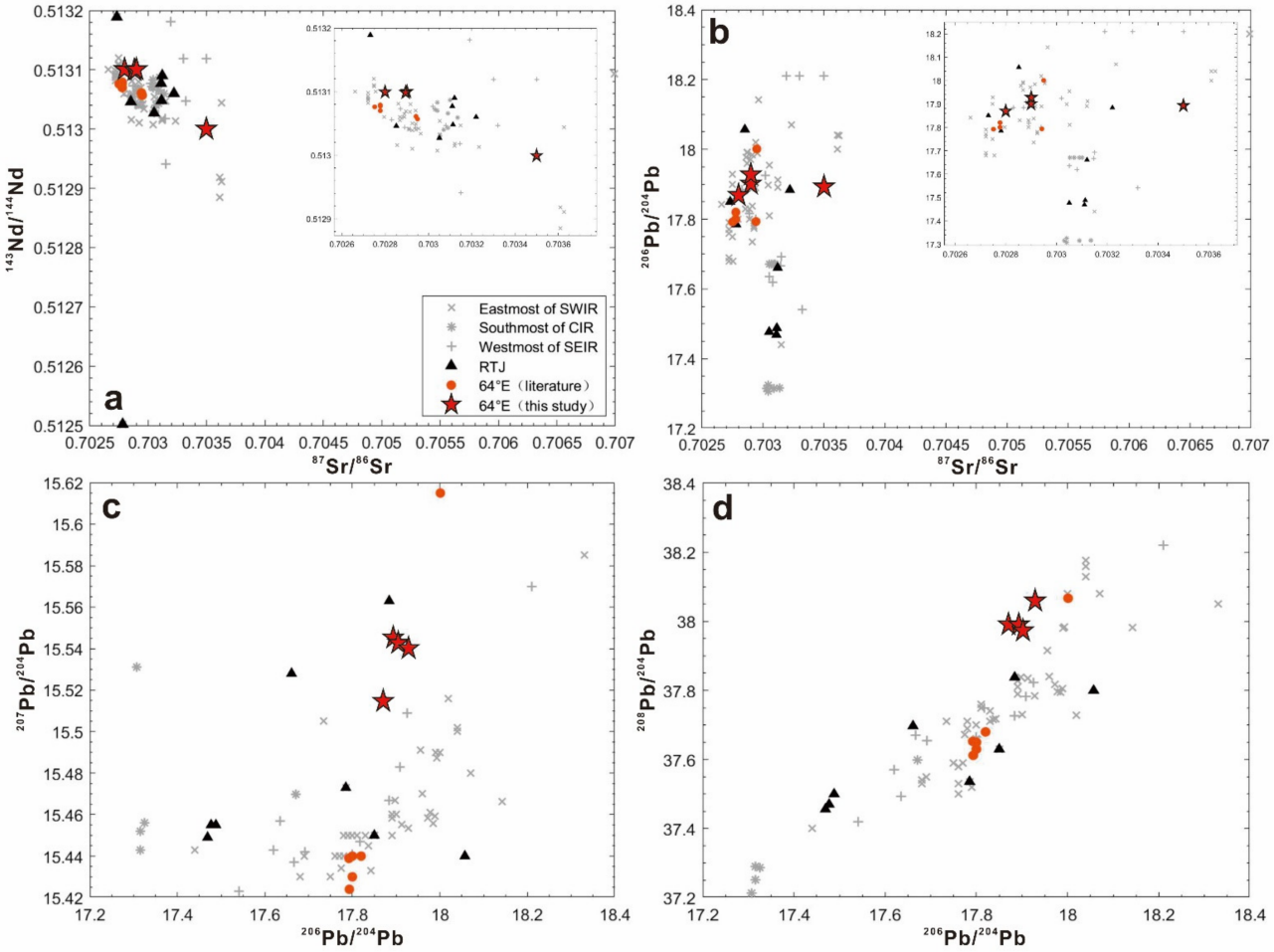

Figure 5. (**a**) $^{87}Sr/^{86}Sr$ vs. $^{143}Nd/^{144}Nd$; (**b**) $^{87}Sr/^{86}Sr$ vs. $^{206}Pb/^{204}Pb$; (**c**) $^{206}Pb/^{204}Pb$ vs. $^{207}Pb/^{204}Pb$; and (**d**) $^{206}Pb/^{204}Pb$ vs. $^{208}Pb/^{204}Pb$ for 64° E MORBs and other 64° E MORBs in the literature [26]. Data of eastern SWIR (E-SWIR), southern Central Indian Ridge (S-CIR), western Southeast Indian Ridge (W-SEIR), and Rodrigues Triple Junction (RTJ) samples are from the PetDB database (http://www.petdb.org/).

6. Discussion

The ultraslow-spreading ridges are characterized by a thicker lithosphere than those of other fast-spreading ridges [33]. MORB samples collected from anomalously thick crusts have been reported for generation processes between 11° E and 15° E-SWIR: JMS (approximately 10 km thick) and Narrowgate segments (approximately 7.5 km thick) [34], and segment #27 (approximately 9.5 km thick) between the Indomed and Gallieni fracture zones [29]. Standish et al. suggested that the crustal thickness variations could be attributed to the oblique spreading, resulting in along-axis melt focusing from beneath magmatic segments to the two magma-robust segments, and the enriched MORB (E-MORB) erupted on the two magma-robust segments was interpreted to result from the melting of a pyroxenite-bearing heterogeneous mantle source [34]. For the case of segment #27, the isotopically enriched N-MORB was interpreted to be the contribution of Crozet plume materials [29]. Moreover, the architectures of high bathymetric and low MBA with a relatively thicker crust occur at the E-SWIR, e.g., #8, #11, #14, etc. [10], which calls for proper explanations for the mantle heterogeneity. Compared with the other segments of SWIR, MORBs sampled along the E-SWIR are distinguished by their higher Na_2O, Sr, and Al_2O_3 compositions, depleted HREE distributions and enriched LREEs.

6.1. Fractional Crystallization

As seen in Table 1, the 64° E basalts have a small compositional range (MgO = 6.73–7.92 wt.%). Although they follow the differentiation trend defined by 50.5° E basalts, they are slightly different from the JMS basalts (Figure 3). The difference in the major element concentrations may result from the change in primary magma composition. Therefore, the fractional crystallization process responsible for the chemical variation of primary magma may reveal the source of mantle heterogeneity.

The 64° E basalts have small amounts of olivine and clinopyroxene phenocrysts, while plagioclase phenocrysts were observed in the samples from the research area as well (Figure 2). Furthermore, most of the 64° E basalts have higher MgO contents (>7 wt.%), indicating that the fractional crystallization of the parent magma is not extensive. The $Mg^{\#}$ of the samples is in the range of 61.93–65.56, indicating the evolution of differentiation from primitive magma ($Mg^{\#}$ = 70) to medium magma ($Mg^{\#}$ = 40) in the process of melt rising [35]. The slightly negative Eu anomaly of the samples (Figure 4) excludes the possibility of significant plagioclase fractional crystallization. The variations of Ni, Cr, and Sr in igneous rocks are sensitive to olivine, clinopyroxene, and plagioclase fractional crystallization from the parent basic magma, respectively [36]. The Sr concentration decreases distinctly with the increase of Y and Zr (Figure 6e,f), indicating a significant process of plagioclase fractional crystallization [37,38]. However, the Ni and Cr concentrations show a distinct positive correlation with the increase of Y and Zr, which is completely different from the other data's trends (i.e., MFZ–RTJ, Indomed Fracture Zone–Gallieni Fracture Zone (IFZ–GFZ), 50.5° E), suggesting that the fractional crystallization of olivine and clinopyroxene of the parent magmas is weak or not significantly relative to plagioclase. This is consistent with the petrographical observation. Overall, the combination of the data of the major and trace elements suggests that the 64° E basalts experienced a minor rather than an extensive magmatic differentiation and probably merely experienced an extensive plagioclase fractional crystallization. This indicates that the plagioclase ultraphyric basalts from 64° E form by plagioclase low-pressure fractional crystallization and accumulation via flotation in a shallow magma chamber [26] contrary to 50.5° E of SWIR (i.e., Duanqiao Seamount) [5,39–41], leading to less magmatic fractionation. It is worth noting that the 64° E basalts have an opposite trend of Ni and Cr versus Y and Zr with MFZ–RTJ, indicating that there may exist differences in primitive magma compositions or mantle heterogeneity beneath the E-SWIR.

6.2. Mantle Melting

The fractionated MORBs preserve information about the source mantle composition and melting. The flat HREE pattern in basalts indicates the absence of residual garnet in its mantle source. The MORBs cannot originate from plagioclase and garnet peridotites but are more likely to originate from the spinel peridotite area [1].

The 64° E samples are characterized with relatively higher SiO_2, Al_2O_3, and Na_2O contents and lower TiO_2, CaO, FeO, and MgO contents than basalts from similar architectures locating at 50.5° E and JMS (Figure 3). The high-Al category MORB has similar characteristics to those of 50.5° E of SWIR, showing lower TiO_2 content. The negative correlations between $Mg^{\#}$ and Al_2O_3 (Figure 7a) suggest that plagioclase is not a major liquid phase. Al is a moderately incompatible element during partial melting. Thus, the high-Al content could result in a lower partial melting degree of mantle peridotite [42]. Previous research on major element compositions [6,43] showed low FeO contents at a given MgO content. Additionally, they are enriched with the most incompatible elements, such as Na_2O (Figure 7b), which is different from the global MORBs' trend because they contain significantly less TiO_2 at a given MgO content. This is inconsistent with the interpretation of lower partial melting.

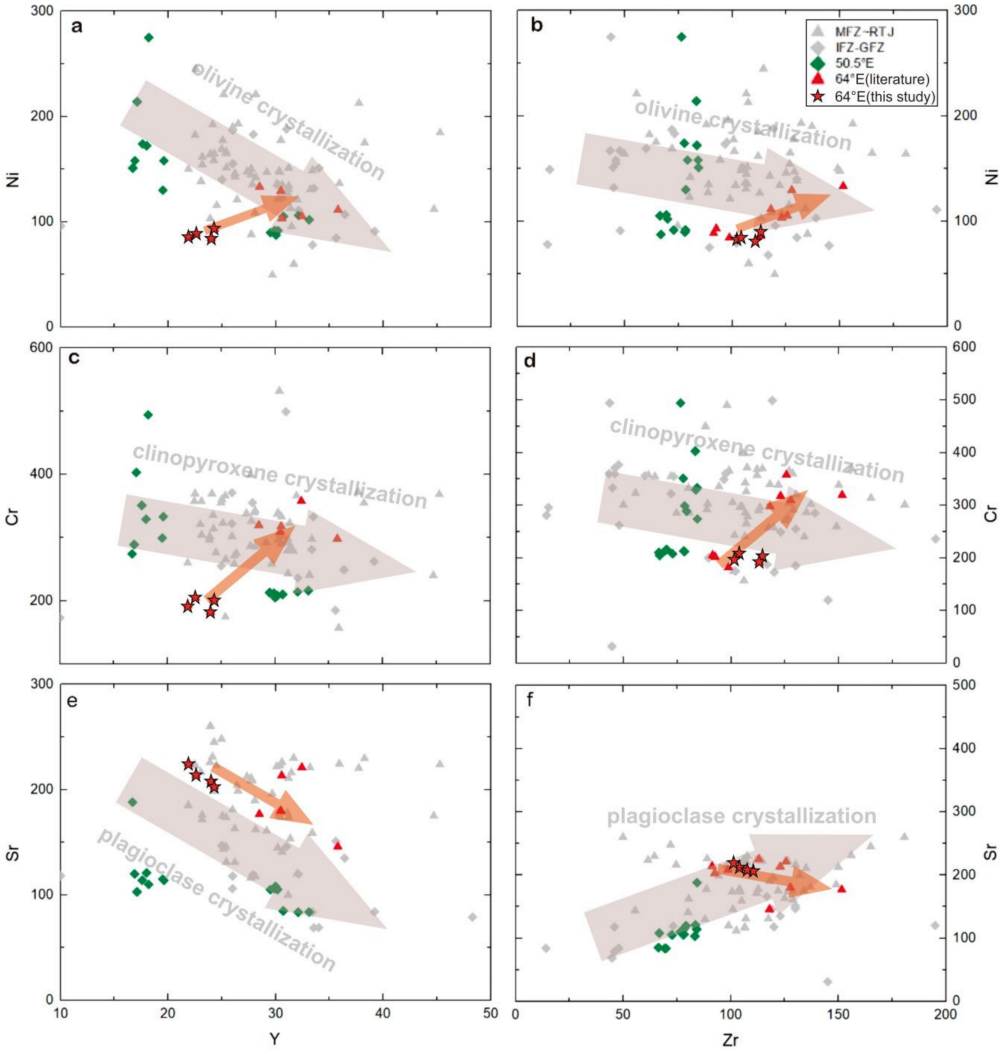

Figure 6. (**a**) Ni, (**c**) Cr, and (**e**) Sr vs. Y and (**b**) Ni; (**d**) Cr, (**f**) Sr vs. Zr diagrams for basalts from 64° E and 50.5° E, with data from Melville Fracture Zone (MFZ) to RTJ and Indomed Fracture Zone–Gallieni Fracture Zone (IFZ to GFZ) as background, respectively. The gray arrow represents the trend of background data, and the red arrow denotes the trend of the 64° E basalts. Data sources are the same as in Figure 4.

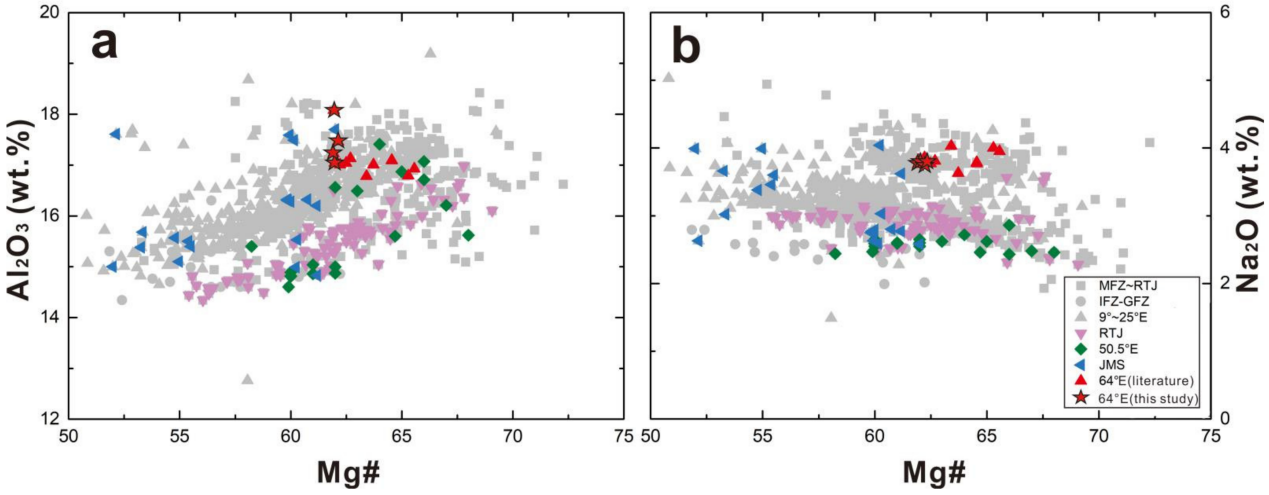

Figure 7. (**a**) Al_2O_3 vs. $Mg^{\#}$ and (**b**) Na_2O vs. $Mg^{\#}$ diagrams for basalts of SWIR. Data sources are the same as in Figure 3.

Any differences in the composition of the source mantle or differences in the degree of partial melting of the mantle with a similar composition may cause differences in the normalized REEs, trace element patterns, and trace element ratios of basalts. Figure 8 shows the covariation of Y/Nb and Zr/Y with Zr/Nb ratios in different domains of SWIR basalts. It shows that the 64° E and 50.5° E could be two typical end-members where the enriched mantle source has low Zr/Nb and Y/Nb with high Zr/Y, while the depleted mantle source has high Zr/Nb and Y/Nb with low Zr/Y.

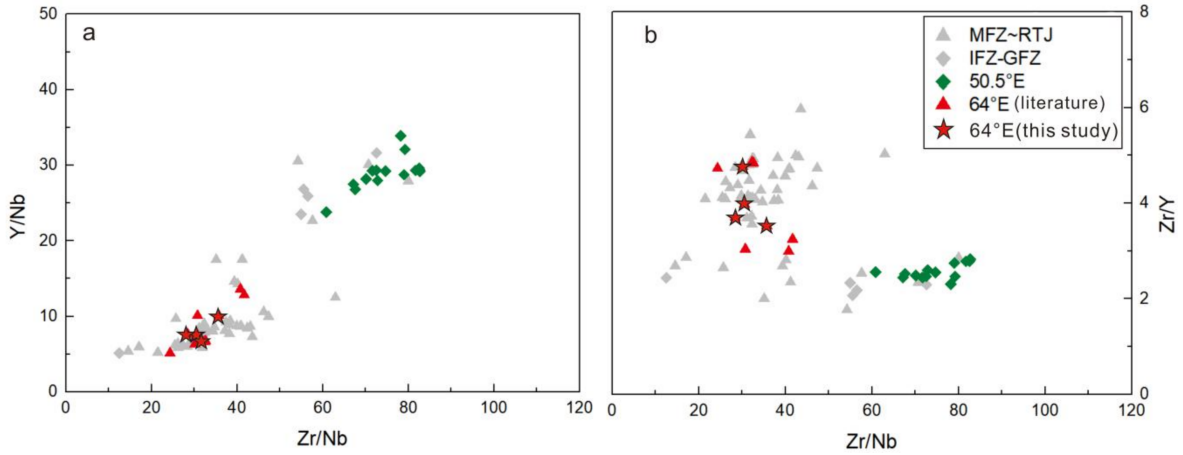

Figure 8. (**a**) Y/Nb vs. Zr/Nb and (**b**) Zr/Y vs. Zr/Nb diagrams for basalts of SWIR. Data sources are the same as in Figure 4.

The Zr, Y, and Nb distribution coefficients between melt and lherzolite residue indicate that Zr/Y and Y/Nb ratios will be more fractionated during low degrees of partial melting than the Zr/Nb ratio [44]. This means that a higher Zr/Y, lower Y/Nb, and slightly lower Zr/Nb ratios should occur by lowering the degree of partial melting. Figure 8 shows that the enriched 64° E basalts have lower Zr/Nb and Y/Nb ratios but higher Zr/Y ratios than the depleted basalts from 50.5° E. Therefore, it is likely that the N-type MORB characteristics from the 64° E originate from the enrichment of a normal, depleted suboceanic mantle by a geochemically enriched component.

6.3. Constraining Mantle Heterogeneity

The variation in the major and trace elements of the basalts from E-SWIR (including 64° E) suggests that the mantle beneath E-SWIR may incorporate some enriched components. The origin and physical form of the enriched components in the mantle source has been a topic of debate [45,46]. Based on the current knowledge of MORB mantle compositions, the enriched mantle source can be either a metasomatized peridotite or a pyroxenite [46–48]. The positive Sr and Eu anomalies probably represent a recycled component in the mantle source [47]. It is worth noting that the positive Sr anomalies are common in the basalts from 64° E whereas the Eu anomalies are absent or not significant (Figure 4). We consider that the positive Sr and Eu anomalies are an inheritance signature of the primary magma. However, these signatures were obscured during magmatic differentiation, because plagioclase fractional crystallization always produces negative Sr and Eu anomalies in magma. As a result, the basalts from 64° E likely represent a mixture of enriched melts derived from an enriched component (e.g., refertilized peridotite or pyroxenite) and depleted melts derived from the mantle peridotite. Meanwhile, this interpretation is consistent with the bimodal melting model suggested by previous studies [6,9,49] in which the primary melt was derived from a mixed mantle source comprising a depleted peridotite and an enriched pyroxenitic lithology.

Previous studies indicated that the mantle beneath the Indian Ocean was contaminated by various enriched components, such as mantle plume material [50], ancient subcontinental lithospheric mantle [51], delaminated continental crust [14,52], and recycled subducted altered oceanic crust and/or sediment [19,53,54]. The ultimate origin of mantle end-member attributes

can be constrained in the Sr–Nd–Pb isotope characteristics. The MORBs from different ridges of Indian Ocean have different isotopic compositions (Figure 9). The E-SWIR basalts (including 64° E) have the largest variation in isotopic composition among RTJ, S-CIR, and W-SEIR basalts, having the highest $^{143}Nd/^{144}Nd$ and radiogenic Pb and the lowest $^{87}Sr/^{86}Sr$. This represents a mixture of an enriched component in the mantle source beneath the E-SWIR [6,9,49]. In addition, the basalts from S-CIR and RTJ show slight variations in Sr and Nd isotope ratios closer to the basalts from E-SWIR (Figure 9a), which indicates an enriched component in the mantle source. The enriched component that contaminates the mantle source is less likely to be hotspot material [50]. It is considered that a depleted MORB mantle (DMM) was variously contaminated by the upper and lower continental crust (UCC and LCC, Supplementary Materials, Figure S1) [52].

As shown in the Pb isotopic plots (Figure 9c,d), most of the E-SWIR basalts (including 64° E) lie on the trend line between the DMM and the LCC (Figure 9d), indicating a more heterogeneous mantle beneath the E-SWIR that may be contaminated by the LCC component, which is consistent with Ray et al. [52]. Furthermore, the $^{207}Pb/^{204}Pb$ values of the E-SWIR basalts (including 64° E) are higher than those of the DMM and LCC, whereas the $^{208}Pb/^{204}Pb$ values are between them. The influence of the hotspot material can also increase the radiogenic Pb and Sr, but the UCC is the most plausible contaminant because the E-SWIR has the highest radiogenic Pb and Nd and is far from the Kerguelen hotspot. Precambrian continental peridotite xenoliths often have unradiogenic Pb similar to LCC [55,56]. Hence, the possibility that the E-SWIR mantle may be contaminated by the ancient continental lithospheric mantle cannot be excluded. However, no matter what the contaminant is, the evidence of contamination by the UCC, LCC, and/or ancient continental lithospheric mantle suggests that the E-SWIR mantle source contains continental lithospheric material.

Most of the isotopic attributes of Indian MORBs on a global scale can be considered using a ternary mixing model involving a depleted mantle of Central Atlantic/Pacific affinity, the common component (i.e., "C") or "focal zone" (FOZO), and a relatively low $^{206}Pb/^{204}Pb$ component, arising from the lower crust [8]. For E-SWIR (including 64° E), axial lavas together with the RTJ, S-CIR, and W-SEIR MORBs define a collinear isotopic array (Figure 9), indicating three principal end-members in the mantle source, i.e., a typical DMM and two other postulated enriched mantles [20,57,58].

Figure 9 shows that the E-SWIR MORBs lie very close to the postulated DMM mantle end-member. Thus, they have the largest amount of the DMM-type components within. With the distance increasing from RTJ, i.e., from the intersection field of SWIR, CIR, and SEIR, there is an isotopic variation related to the DMM-type component's dilution in the mantle due to the effect of ridge section [59]. The S-CIR MORBs overlap with RTJ but are different from the E-SWIR samples, implying less FOZO and C-type and more enriched mantle components beneath its axis (Figure 9b,d). This also confirms that the CIR mantle is contaminated by the LCC and/or UCC components [52]. The MORBs exhibit a wide range of isotopic compositions in W-SEIR, indicating that the DMM source has been variably contaminated by the FOZO and C-type component (Figure 9a). The 64° E samples are close in composition to the DMM end-member and overlap with the field of E-SWIR with the least LCC-like signature. A stranded LCC is embedded in the upper mantle [14]. Even though the ~64° E samples are far from the known hotspot (e.g., Kerguelen hotspot). The mantle source still maintains an LCC- and/or EM2-like signature (Figure 9c,d). Additionally, we show that some samples plot along the mixing region among DMM, LCC, and EM2 in the $^{206}Pb/^{204}Pb$ versus $^{207}Pb/^{204}Pb$ and $^{208}Pb/^{204}Pb$ plots, indicating a small portion of LCC and EM2 components in the mantle source.

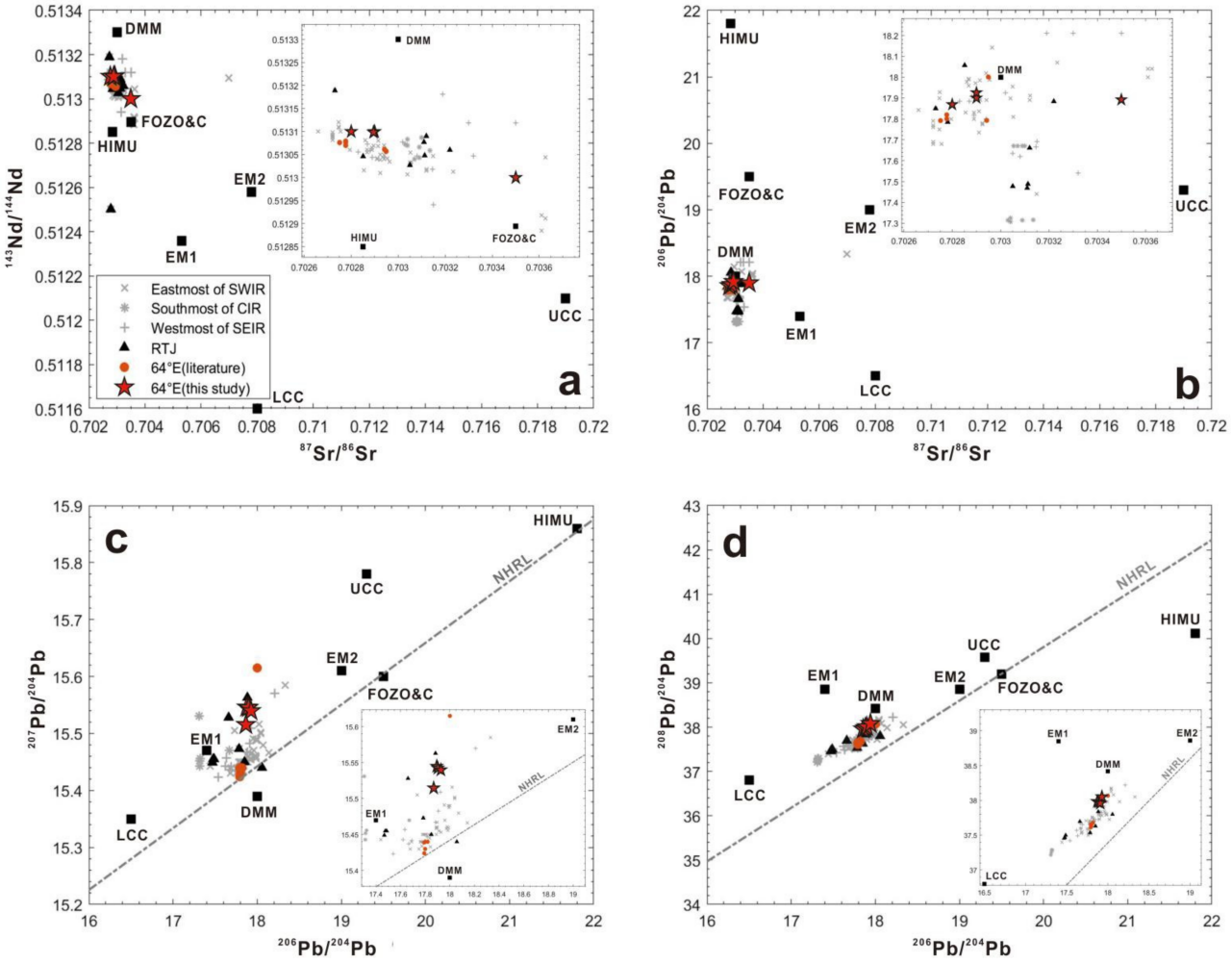

Figure 9. Isotope ratio diagrams showing the 64° E, E-SWIR, S-CIR, W-SEIR, and RTJ basalts along with different mantle end-members. (**a**) $^{87}Sr/^{86}Sr$ versus $^{143}Nd/^{144}Nd$; (**b**) $^{87}Sr/^{86}Sr$ versus $^{206}Pb/^{204}Pb$; (**c**) $^{206}Pb/^{204}Pb$ versus $^{207}Pb/^{204}Pb$; and (**d**) $^{206}Pb/^{204}Pb$ versus $^{208}Pb/^{204}Pb$. Data sources are the same as in Figure 5. Isotopic data sources for depleted MORB mantle (DMM) are from [20] and other mantle end-members (i.e., EM1, EM2, and high-U/Pb mantle (HIMU)) are from [57]. Composition of proposed mantle end-member C is from [58]. The lower continental crust (LCC) composition is from [51], and the upper crustal composition (i.e., UCC) is from [36]. NHRL denotes the Northern Hemisphere Reference Line [20].

To determine the number of mantle sources for 64° E of the SWIR basalts, we performed principal component analysis (PCA) on the Pb isotopic compositions for 64° E of SWIR and its adjacent areas (i.e., E-SWIR, S-CIR, W-SEIR, and RTJ) MORBs (Supplementary Materials, PCA S1). The source materials of lavas are often referred to as components because the orthogonal coordinates are produced by PCA. For simplicity, we refer to the orthogonal coordinates produced by PCA as "principal components." The first and second principal components account for 89% and 9.9% of the variance, respectively, while the third principal component accounts for only 1.1% of the variance (Figure 10a). Supposing that we consider the Pb data from the comparison areas, then the dominance of the first principal component is even more striking (92.9%), and the contribution of the third principal component almost vanishes (1.1%) (Figure 10b). Thus, one mantle source dominates most of the variability, with two minor sources involved. In the PCA diagrams (Figure 10a), we can observe that the mantle source region gradually undergoes binary or ternary mixing from 61° E of SWIR eastward to RTJ. This variety is attributed to the progression of a distinct SWIR mantle eastward in response to the migration of RTJ [17]. In the PCA diagrams (Figure 10b), 64° E samples plot below the axis of the first principal component and to the right of the second principal component axis. Most of the E-SWIR samples (40.7%, n = 22) plot above the

first principal component axis and to the left of the second principal component axis. By contrast, the S-CIR samples plot below the first principal component axis and to the left of the second principal component axis, different from the others. Moreover, the RTJ and W-SEIR samples are located in between. The third mantle source's hint is visible because the samples are not perfectly aligned along the first principal component but scattered by the second principal component.

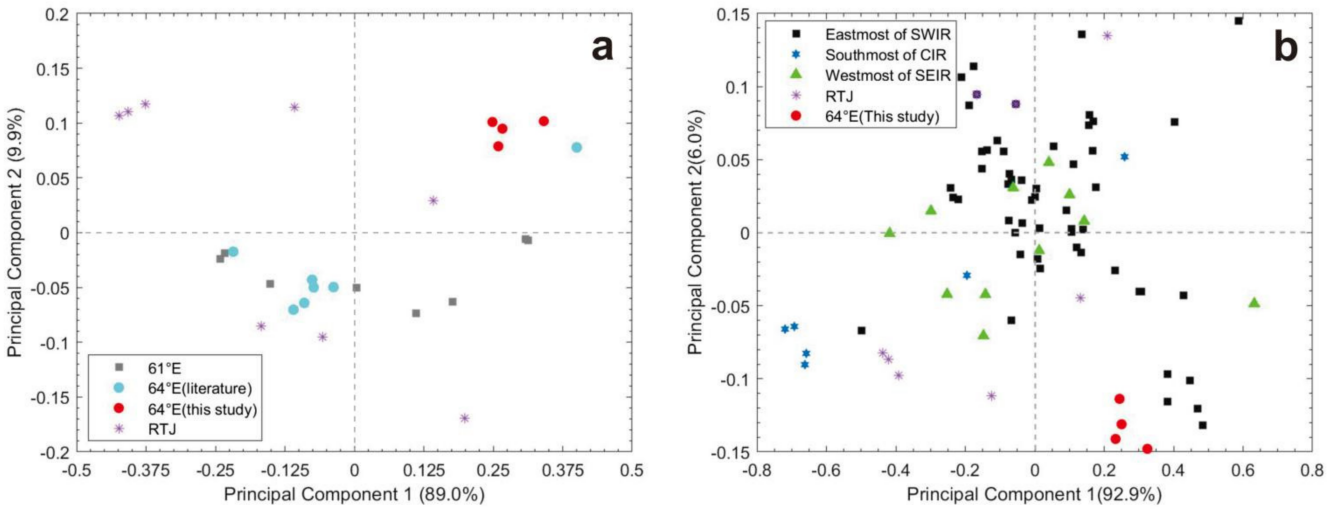

Figure 10. Principal component analysis (**a**) restricted to the 61° E, 64° E, and RTJ Pb isotopic data and (**b**) applied to all the Pb isotopic data (this study and data from the literature). Data sources are the same as in Figure 5.

To distinguish from binary and ternary mixing, we conducted the PCA of the Pb isotopic compositions for the E-SWIR samples (including 64° E of this study) and MORBs from the S-CIR, W-SEIR, and RTJ (Figure 11). Results show that 99% of the variance is accounted for by the first two principal components (85.2% for the first principal component and 13.8% for the second principal component). This means that the Pb data are located on a plane in the three-dimensional $^{206}Pb/^{204}Pb$ versus $^{207}Pb/^{204}Pb$ versus $^{208}Pb/^{204}Pb$ space. Figure 11 shows that the data are orthogonally projected on this plane defined by the two principal components. The MORBs from the 64° E samples are more depleted than the lavas from other regions, such as S-CIR and W-SEIR. The MORBs from E-SWIR, W-SEIR, and RTJ represent a ternary mixing as they do not plot along a line but rather within the triangle defined by the three, mantle end-members for DMM, LCC, and EM2.

Figure 11. shows the interaction among SWIR, CIR, and SEIR with ternary mixing mantle end-members. The influence of CIR and SEIR on SWIR is not localized on a specific section such as the RTJ region but on the entire Melville–RTJ segment. Thus, its isotopic signature is less pronounced than what is observed for other ridge–ridge interactions. We suggest that CIR- and SEIR-derived materials contaminate the upper mantle below E-SWIR (including 64° E and RTJ). This contamination of the Indian Ocean mantle was possibly related to the third stage of the Gondwana breakup during 155–135 Ma when strike–slip movement along a mega fracture, belonging to the Davie Transform Faults within the Somali basin, split Gondwanaland into the East and West Gondwana plates [54,60–62]. This result also reveals that significant interactions occurred between the continental lithosphere and oceanic mantle during the opening of the Indian Ocean, suggesting that continental material played a significant role in producing the isotopic anomaly observed in the Indian Ocean MORBs.

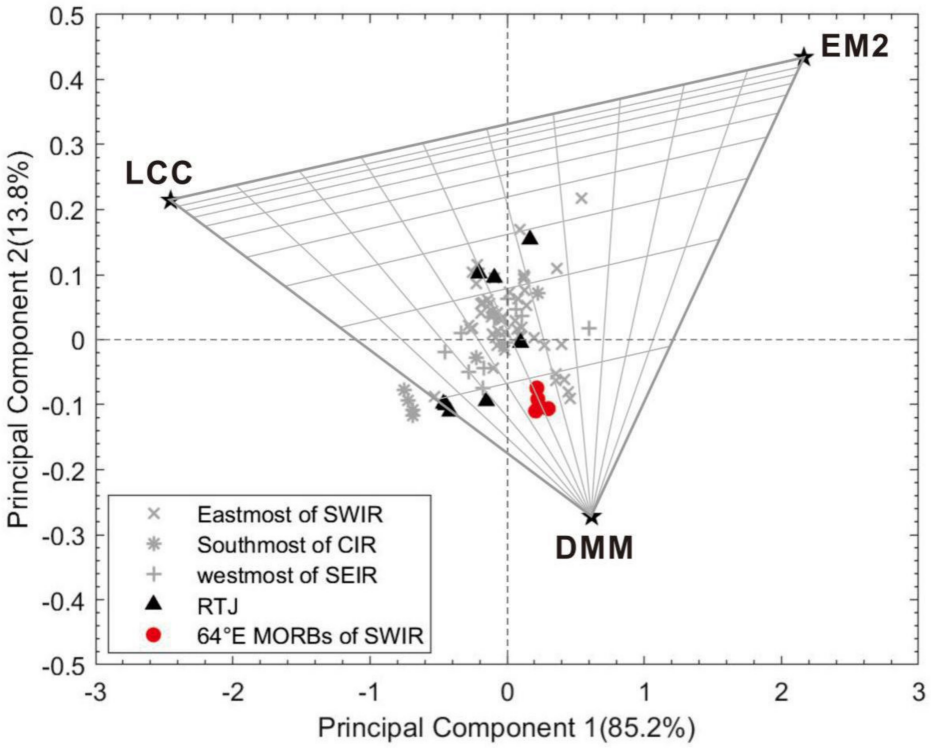

Figure 11. PCA of the $^{206}Pb/^{204}Pb$, $^{207}Pb/^{204}Pb$, and $^{208}Pb/^{204}Pb$ data. The first principal component explains 85.2% of the total variability of the data, and the second principal component explains 13.8% of this variability. Hence, this two-dimensional representation of the three-dimensional dataset shows 99.0% of the total variability. The triangular pattern defined by the samples in this diagram is consistent with the proposed ternary mixing between DMM, LCC, and EM2.

7. Conclusions

The basalts from the 64° E show high contents of Al_2O_3, weak depletion in HREE patterns, and enrichment in the LILEs. In contrary to high $^{143}Nd/^{144}Nd$ and Pb isotopes, the $^{87}Sr/^{86}Sr$ is comparably low. From petrographic analysis and trace element characteristics, we found that the MORB samples undergo crystallization of plagioclase of the parent magmas in the shallow crust. By contrast, the fractional crystallization of olivine and clinopyroxene is not significant. Incompatible trace elements and isotopic characteristics show that the basaltic melt in this area was formed by the partial melting of lherzolite, probably originating from the stable field of spinel peridotite.

The negative correlation between Zr/Nb and Zr/Y suggests a geochemically heterogeneous mantle source. Through comprehensive comparisons of the Sr–Nd–Pb isotopic characteristics of E-SWIR, S-CIR, W-SEIR, and RTJ, we found that the Indian Ocean ridge system, especially in the RTJ region, experienced a complex mantle source mixing process and formed various types of MORBs. Furthermore, we confirmed that the DMM is unevenly contaminated by the LCC- and enriched-EM2-like components, genetically related to the Gondwana breakup, and contaminated by both the upper and lower continental crust (or continental mantle) components.

Supplementary Materials: The following are available online at https://www.mdpi.com/2075-163X/11/2/175/s1, Figure S1: Plots of εSr vs. εNd showing data for DMM and LCC end-members. Data sources are the same as in Figure 5; PCA S1: Principal component analysis

Author Contributions: Conceptualization, J.L. and C.T.; methodology, J.L. and Z.D.; validation, J.L. and C.T.; formal analysis, Z.D.; investigation, Z.D.; resources, C.T.; data curation, Z.D.; writing—original draft preparation, Z.D. and J.L.; writing—review and editing, J.L., S.L., and W.L.; visualization, Z.D., J.L., and G.Z.; supervision, S.L. and W.L.; project administration, C.T.; funding acquisition, C.T. All authors have read and agreed to the published version of the manuscript.

Funding: This study was financially supported by the National Key Research and Development Program of China nos. 2017YFC0306603, 2016YFC0304905, and 2019YFC1408705; the National Science Foundation of China (grant no. 41806076 and no. 41906174); and the China Ocean Mineral Resources R & D Association (COMRA) Major Project under contract nos. DY135-S1-1-01 and DY135-S1-1-02.

Institutional Review Board Statement: Not applicable.

Informed Consent Statement: Not applicable.

Data Availability Statement: Not applicable.

Acknowledgments: We thank the captain and crew of the Leg II of the 35th COMRA Cruise on R/V XiangYangHong 9 and the submersible Jiaolong group. Sr–Nd–Pb isotopes analyses were kindly done by Fukun Chen and Ping Xiao from the Laboratory for Radiogenic Isotope Geochemistry, School of Earth and Space Science, University of Science and Technology of China. We appreciate two anonymous reviewers for their constructive comments and suggestions.

Conflicts of Interest: The authors declare no conflict of interest.

References

1. Dick, H.J.B.; Lin, J.; Schouten, H. An ultraslow-spreading class of ocean ridge. *Nature* **2003**, *426*, 405–412. [CrossRef]
2. Royer, J.-Y.P.; Philippe, B.H.; Scotese, W.; Christopher, R. Evolution of the Southwest Indian Ridge from the Late Cretaceous (anomaly 34) to the Middle Eocene (anomaly 20). *Tectonophysics* **1988**, *155*, 235–260. [CrossRef]
3. Searle, R.C.; Bralee, A.V. Asymmetric generation of oceanic crust at the ultra-slow spreading Southwest Indian Ridge, 64° E. *Geochem. Geophys. Geosyst.* **2007**, *8*. [CrossRef]
4. Cannat, M.; Rommevaux-Jestin, C.; Fujimoto, H. Melt supply variations to a magma-poor ultra-slow spreading ridge (Southwest Indian Ridge 61° to 69° E). *Geochem. Geophys. Geosyst.* **2003**, *4*. [CrossRef]
5. Sauter, D.; Cannat, M.; Roumejon, S.; Andreani, M.; Birot, D.; Bronner, A.; Brunelli, D.; Carlut, J.; Delacour, A.; Guyader, V.; et al. Continuous exhumation of mantle-derived rocks at the Southwest Indian Ridge for 11 million years. *Nat. Geosci.* **2013**, *6*, 314–320. [CrossRef]
6. Meyzen, C.M.; Toplis, M.J.; Humler, E.; Ludden, J.N.; Mevel, C. A discontinuity in mantle composition beneath the southwest Indian ridge. *Nature* **2003**, *421*, 731–733. [CrossRef]
7. Seyler, M.; Cannat, M.; Mevel, C. Evidence for major-element heterogeneity in the mantle source of abyssal peridotites from the Southwest Indian Ridge (52° to 68° E). *Geochem. Geophys. Geosyst.* **2003**, *4*. [CrossRef]
8. Font, L.; Murton, B.J.; Roberts, S.; Tindle, A.G. Variations in melt productivity and melting conditions along SWIR (70–49° E): Evidence from olivine-hosted and plagioclase-hosted melt inclusions. *J. Petrol.* **2007**, *48*, 1471–1494. [CrossRef]
9. Paquet, M.; Cannat, M.; Brunelli, D.; Hamelin, C.; Humler, E. Effect of melt/mantle interactions on MORB chemistry at the easternmost Southwest Indian Ridge (61°–67° E). *Geochem. Geophys. Geosyst.* **2016**, *17*, 4605–4640. [CrossRef]
10. Cannat, M.; Rommevaux-Jestin, C.; Sauter, D.; Deplus, C.; Mendel, V. Formation of the axial relief at the very slow spreading Southwest Indian Ridge (49° to 69° E). *J. Geophys. Res.* **1999**, *104*, 22825–22843. [CrossRef]
11. Francis, T.J.G.; Raitt, R.W. Seismic refraction measurements in the southern Indian Ocean. *J. Geophys. Res.* **1967**, *72*, 3015–3041. [CrossRef]
12. Minshull, T.A.; White, R.S. Thin Crust on the Flanks of the Slow-Spreading Southwest Indian Ridge. *Geophys. J. Int.* **1996**, *125*, 139–148. [CrossRef]
13. Muller, M.R.; Minshull, T.A.; White, R.S. Segmentation and melt supply at the Southwest Indian Ridge. *Geology* **1999**, *27*, 867–870. [CrossRef]
14. Meyzen, C.M.; Ludden, J.N.; Humler, E.; Luais, B.; Toplis, M.J.; Mével, C.; Storey, M. New insights into the origin and distribution of the DUPAL isotope anomaly in the Indian Ocean mantle from MORB of the Southwest Indian Ridge. *Geochem. Geophys. Geosyst.* **2005**, *6*. [CrossRef]
15. Michard, A.; Montigny, R.; Schlich, R. Geochemistry of the mantle beneath the Rodriguez Triple Junction and the South-East Indian Ridge. *Earth Planet. Sci. Lett.* **1986**, *78*, 1–114. [CrossRef]
16. Price, R.C.; Kennedy, A.K.; Riggs-Sneeringer, M.; Frey, F.A. Geochemistry of basalts from the Indian ocean triple junction: Implications for the generation and evolution of Indian Ocean ridge basalts. *Earth Planet. Sci. Lett.* **1986**, *78*, 379–396. [CrossRef]
17. Mahoney, J.J.; Natland, J.H.; White, W.M.; Poreda, R.; Bloomer, S.H.; Fisher, R.L.; Baxter, A.N. Isotopic and geochemical provinces of the western Indian Ocean spreading centers. *J. Geophys. Res.* **1989**, *94*, 4033–4052. [CrossRef]
18. Mahoney, J.J.; le Roex, A.P.; Peng, Z.; Fisher, R.L.; Natland, J.H. Southwestern limits of Indian Ocean Ridge mantle and the origin of low $^{206}Pb/^{204}Pb$ mid-ocean ridge basalts: Isotope systematics of the Southwest Indian Ridge (17°–50° E). *J. Geophys. Res.* **1992**, *97*, 19771–19790. [CrossRef]
19. Dupré, B.; Allégre, C.J. Pb-Sr isotope variation in Indian Ocean basalts and mixing phenomena. *Nature* **1983**, *303*, 142–146. [CrossRef]
20. Hart, S.R. A large-scale isotope anomaly in the Southern Hemisphere mantle. *Nature* **1984**, *309*, 753–757. [CrossRef]

21. Sauter, D.; Carton, H.; Mendel, V.; Munschy, M.; Rommevaux-Jestin, C.; Schott, J.J.; Whitechurch, H. Ridge segmentation and the magnetic structure of the Southwest Indian Ridge (at 50°30′ E, 55°30′ E and 66°20′ E): Implications for magmatic processes at ultraslow-spreading centers. *Geochem. Geophys. Geosyst.* **2004**, *5*, 374–378. [CrossRef]
22. Sauter, D.; Mendel, V.; Rommevaux-Jestin, C.; Parson, L.M.; Fujimoto, H.; Mevel, C.; Cannat, M.; Tamaki, K. Focused magmatism versus amagmatic spreading along the ultra-slow spreading Southwest Indian Ridge: Evidence from TOBI side scan sonar imagery. *Geochem. Geophys. Geosyst.* **2004**, *5*. [CrossRef]
23. Seyler, M.; Brunelli, D.; Toplis, M.J.; Mével, C. Multiscale chemical heterogeneities beneath the eastern Southwest Indian Ridge (52°–68° E): Trace element compositions of along-axis dredged peridotites. *Geochem. Geophys. Geosyst.* **2011**, *12*. [CrossRef]
24. Chen, J.; Tao, C.; Liang, J.; Liao, S.; Dong, C.; Li, H.; Li, W.; Wang, Y.; Yue, X.; He, Y. Newly discovered hydrothermal fields along the ultraslow-spreading Southwest Indian Ridge around 63° E. *Acta Oceanol. Sin.* **2018**, *37*, 61–67. [CrossRef]
25. Mendel, V.; Sauter, D.; Parson, L.; Vanney, J.R. Segmentation and morphotectonic variations along a super slow-spreading center: The Southwest Indian Ridge (57°–70° E). *Mar. Geophys. Res.* **1997**, *19*, 505–533. [CrossRef]
26. Li, W.; Tao, C.H.; Zhang, W. Melt Inclusions in Plagioclase Macrocrysts at Mount Jourdanne, Southwest Indian Ridge (~64° E): Implications for an Enriched Mantle Source and Shallow Magmatic Processes. *Minerals* **2019**, *9*, 493. [CrossRef]
27. Sauter, D.; Parson, L.; Mendel, V.; Rommevaux-Jestin, C.; Gomez, O.; Briais, A.; Mevel, C.; Tamaki, K.; Team, F.S. TOBI sidescan sonar imagery of the very slow-spreading Southwest Indian Ridge: Evidence for along-axis magma distribution. *Earth Planet. Sci. Lett.* **2002**, *202*, 511–512. [CrossRef]
28. Ding, T.; Tao, C.; Dias, G.A.; Liang, J.; Huang, H. Sulfur isotopic compositions of sulfides along the southwest indian ridge: Implications for mineralization in ultramafic rocks. *Miner. Depos.* **2020**. [CrossRef]
29. Yang, A.Y.; Zhao, T.P.; Zhou, M.F.; Deng, X.G. Isotopically enriched N-MORB-a new geochemical signature of off-axis plume-ridge interaction: A case study at 50°28′E, Southwest Indian Ridge. *J. Geophys. Res.* **2017**, *122*, 191–213. [CrossRef]
30. Sun, S.-S.; McDonough, W.F. Chemical and isotopic systematics of oceanic basalts: Implications for mantle composition and processes. *Geol. Soc.* **1989**, *42*. [CrossRef]
31. Roex, A.P.L.; Dick, H.J.B.; Watkins, R.T. Petrogenesis of anomalous K-enriched MORB from the Southwest Indian Ridge: 11°53′ E to 14°38′ E. *Contrib. Mineral. Petrol.* **1992**, *110*, 253–268. [CrossRef]
32. Shimizu, K.; Ito, M.; Chang, Q.; Miyazaki, T.; Kimura, J.I. Identifying volatile mantle trend with the water–fluorine–cerium systematics of basaltic glass. *Chem. Geol.* **2019**, *522*, 283–294. [CrossRef]
33. Bown, J.W.; White, R.S. Variation with spreading rate of oceanic crustal thickness and geochemistry. *Earth Planet. Sci. Lett.* **1994**, *121*, 435–439. [CrossRef]
34. Standish, J.J.; Dick, H.J.B.; Michael, P.J.; Melson, W.G.; O'Hearn, T. MORB generation beneath the ultraslow spreading Southwest Indian Ridge (9–25° E): Major element chemistry and the importance of process versus source. *Geochem. Geophys. Geosyst.* **2008**, *9*. [CrossRef]
35. Le Roex, A.P.; Dick, J.B.H.; Fisher, L.R. Petrology and Geochemistry of MORB from 25° E to 46° E along the Southwest Indian Ridge: Evidence for Contrasting Styles of Mantle Enrichment. *J. Petrol.* **1989**, *30*, 947–986. [CrossRef]
36. Hemming, S.R.; Mclennan, S.M. Pb isotope compositions of modern deep sea turbidites. *Earth Planet. Sci. Lett.* **2001**, *184*, 489–503. [CrossRef]
37. Blundy, J.D.; Robinson, J.A.C.; Wood, B.J. Heavy REE are compatible in clinopyroxene on the spinel lherzolite solidus. *Earth Planet. Sci. Lett.* **1998**, *160*, 493–504. [CrossRef]
38. Pandey, S.K.; Pal, S.; Shrivastava, J.P.; Roonwal, G.S. Trace elements geochemistry and petrogenesis of basalt from the southern part of the East Pacific Rise. *J. Geol. Soc. India* **2013**, *81*, 91–100. [CrossRef]
39. Li, J.; Jian, H.; Chen, Y.J.; Singh, S.C.; Ruan, A.; Qiu, X. Seismic observation of an extremely magmatic accretion at the ultraslow spreading southwest indian ridge. *Geophys. Res. Lett.* **2015**, *42*, 2656–2663. [CrossRef]
40. Niu, X.; Ruan, A.; Li, J.; Minshull, T.A.; Sauter, D.; Wu, Z. Along-axis variation in crustal thickness at the ultraslow spreading southwest indian ridge (50° E) from a wide-angle seismic experiment. *Geochem. Geophys. Geosyst.* **2015**, *16*, 468–485. [CrossRef]
41. Jian, H.; Singh, S.C.; Chen, Y.J.; Li, J. Evidence of an axial magma chamber beneath the ultraslow-spreading southwest indian ridge. *Geology* **2017**, *45*, G38356.1. [CrossRef]
42. Gale, A.; Langmuir, C.H.; Dalton, C.A. The Global Systematics of Ocean Ridge Basalts and their Origin. *J. Petrol.* **2014**, *55*, 1051–1082. [CrossRef]
43. Cannat, M.; Sauter, D.; Bezos, A.; Meyzen, C.; Humler, E.; Le Rigoleur, M. Spreading rate, spreading obliquity, and melt supply at the ultraslow spreading Southwest Indian Ridge. *Geochem. Geophys. Geosyst.* **2008**, *9*. [CrossRef]
44. Pearce, J.A.; Norry, M.J. Petrogenetic implications of Ti, Zr, Y, and Nb variations in volcanic rocks. *Contrib. Mineral. Petrol.* **1979**, *69*, 33–47. [CrossRef]
45. Hirschmann, M.; Stolper, E. A possible role for garnet pyroxenite in the origin of the 'garnet signature' in MORB. *Contrib. Mineral. Petrol.* **1996**, *124*, 185–208. [CrossRef]
46. Sobolev, A.V.; Hofmann, A.W.; Kuzmin, D.V.; Yaxley, G.M.; Arndt, N.T.; Chung, S.L.; Danyushevsky, L.V.; Elliott, T.; Frey, F.A.; Garcia, M.O.; et al. The amount of recycled crust in sources of mantle-derived melts. *Science* **2007**, *316*, 412–417. [CrossRef]
47. Le Roux, P.J.; le Roex, A.P.; Schilling, J.G.; Shimizu, N.; Perkins, W.W.; Pearce, N.J.G. Mantle heterogeneity beneath the southern Mid-Atlantic Ridge: Trace element evidence for contamination of ambient asthenospheric mantle. *Earth Planet. Sci. Lett.* **2002**, *203*, 479–498. [CrossRef]

48. Zhang, G.; Zong, C.; Yin, X.; Li, H. Geochemical constraints on a mixed pyroxenite-peridotite source for East Pacific Rise basalts. *Chem. Geol.* **2012**, *330–331*, 176–187. [CrossRef]
49. Paquet, M.; Cédric, H.; Moreira, M.; Cannat, M. The isotopic (He, Ne, Sr, Nd, Hf, Pb) signature in the indian mantle over 8.8 Ma. *Chem. Geol.* **2020**, *550*, 119741. [CrossRef]
50. Nauret, F.; Abouchami, W.; Galer, S.J.G.; Hofmann, A.W.; Hémond, C.; Chauvel, C. Correlated trace element-Pb isotope enrichments in Indian MORB along 18–20° S, Central Indian Ridge. *Earth Planet. Sci. Lett.* **2006**, *245*, 137–152. [CrossRef]
51. Escrig, S.; Capmas, F.; Dupre, B.; Allegre, C. Osmium isotopic constraints on the nature of the dupal anomaly from indian mid-ocean-ridge basalts. *Nature* **2004**, *431*, 59–63. [CrossRef]
52. Ray, D.; Misra, S.; Banerjee, R. Geochemical variability of MORBs along slow to intermediate spreading Carlsberg—Central Indian Ridge, Indian Ocean. *J. Asian Earth Sci.* **2013**, *S70–S71*, 125–141. [CrossRef]
53. Cohen, R.S.; O'Nions, R.K. The lead, neodymium and strontium isotopic structure of ocean ridge basalts. *J. Petrol.* **1982**, *23*, 299–324. [CrossRef]
54. Rehkämper, M.; Hofmann, A.W. Recycled ocean crust and sediment in Indian Ocean MORB. *Earth Planet. Sci. Lett.* **1997**, *147*, 93–106. [CrossRef]
55. Rudnick, R.L.; Goldstein, S.L. The Pb isotopic compositions of lower crustal xenoliths and the evolution of lower crustal Pb. *Earth Planet. Sci. Lett.* **1990**, *36*, 203–225. [CrossRef]
56. Chen, W.; Arculus, R.J. Geochemical and isotopic characteristics of lower crustal xenoliths, San Francisco Volcanic Field, Arizona, USA. *Lithos* **1995**, *36*, 203–225. [CrossRef]
57. Armienti, P.; Gasperini, D. Do We Really Need Mantle Components to Define Mantle Composition? *J. Petrol.* **2007**, *4*, 693–709. [CrossRef]
58. Hanan, B.B.; Graham, D.W. Lead and Helium Isotope Evidence from Oceanic Basalts for a Common Deep Source of Mantle Plumes. *Science* **1996**, *272*, 991–995. [CrossRef] [PubMed]
59. Niu, Y.; Hékinian, R. Ridge suction drives plume-ridge interactions. In *Oceanic Hotspots*; Springer: Berlin/Heidelberg, Germany, 2004.
60. Norton, I.O.; Sclater, J.G. A model for the evolution of the Indian Ocean and the break up of Gondwanaland. *J. Geophys. Res.* **1979**, *84*, 6803–6830. [CrossRef]
61. Kamanetsky, V.S.; Mass, R.; Sushchevskaya, N.M.; Norman, M.D.; Cartwright, I.; Peyve, A.A. Remnants of Gondwana continental lithosphere in oceanic upper mantle: Evidence from the South Atlantic Ridge. *Geology* **2001**, *29*, 243–246. [CrossRef]
62. Weis, D.; Ingle, S.; Damasceno, D.; Frey, F.A.; Nicolaysen, K.; Barling, J. Leg 183 Shipboard Scientific Party. Origin of continental components in Indian Ocean basalts: Evidence from Elan Bank (Kerguelen Plateau, ODP Leg 183, Site 1137). *Geology* **2001**, *29*, 147–150. [CrossRef]